Mapana – Journal of Sciences
2025, Vol. 24, No. 2, *11-32*
ISSN 0975-3303 | https://doi.org/10.12723/mjs.73.2

Synthesis, Structural Characterization, and Quantum Chemical Analysis of (E)-2-(1-(4-Bromophenyl)ethylidene)hydrazinecarbothioamide: A Potential Candidate for Biological Applications

R. R. Saravanan*, M. Karthika*, H. Aafiya Shameem* and R. Mendoza-Meroño†

Abstract

This study reports the synthesis, structural characterisation, and computational analysis of a novel compound, (E)-2-(1-(4-bromophenyl)ethylidene)hydrazine (EBEHC), synthesised via condensation of 1-(4-bromophenyl) ethanone and thiosemicarbazide in methanol. Yellow single crystals were obtained through recrystallisation. Single-crystal X-ray diffraction revealed that EBEHC crystallises in a monoclinic system (space group P21/c), with a unit cell volume of 1103.56 Å^3. Experimental and DFT-calculated geometries showed a strong correlation, with bond length and angle deviations within 0.02 Å and 3°, respectively. Conformational analysis identified R1(a) as the most stable conformer (energy: -9147715.587 kJ/mol), while R2(b) was the least stable (ΔE: +2874.87 kJ/mol). FT-IR and DFT analyses confirmed N–H stretching near 3444 cm^{-1} and C–Br vibrations near 445 cm^{-1}. Hirshfeld surface analysis revealed significant intermolecular interactions—hydrogen bonding (45.2%) and halogen contacts (19.4%). Molecular docking indicated favourable binding with cholesterol-reducing targets, suggesting potential anti-cholesterol properties. These findings highlight EBEHC's promising structural, spectroscopic, and biological characteristics for future therapeutic applications.

Keywords: EBEHC, HMG-CoA, Hirshfeld Surface Analysis, FT-IR, FT-Raman

---

* Department of Physics, Bon Secours College for Women (Autonomous) (Affiliated to Bharathidasan University, Tiruchirappalli), Thanjavur, Tamil Nadu, India; saravapj@gmail.com

† Faculty of Chemistry, Department of Physical and Analytical Chemistry, University Oviedo, C/ Julian Claveria, 8, 33006 Oviedo, Asturias, Spain

1. Introduction

Myocardial infarction (MI), commonly referred to as a heart attack, is the leading cause of death worldwide. It occurs due to an inadequate blood supply to the heart muscle, resulting in myocardial necrosis. Various risk factors, including a sedentary lifestyle, stress, smoking, alcohol consumption, obesity, diabetes, and hypertension, contribute to the development of MI. Additionally, conditions such as hypercholesterolemia, hyperlipidemia, and hypertriglyceridemia collectively promote atherosclerosis, which increases the risk of MI [1]. Studies also highlight the critical roles of lipid-metabolising enzymes in MI progression. For instance, HMG-CoA reductase and lipoprotein lipase (LPL) are key contributors to the disease's development. Conversely, lecithin cholesterol acyltransferase (LCAT), an enzyme that esterifies cholesterol on the surface of high-density lipoprotein cholesterol (HDL-C), facilitates the formation of large HDL-C particles. These particles play a protective role against cardiovascular diseases (CVD)[2]. Heart failure following myocardial infarction (MI) has been shown to be associated with antioxidant deficiencies and increased myocardial oxidative stress[3]. Bioinformatics, a computational approach, is widely used to address biological challenges through structural predictions and molecular docking studies involving biomolecules such as genes, nucleic acids, and proteins. Molecular docking software plays a crucial role in drug design by evaluating and predicting the binding interactions of drugs with the active sites of enzymes. Based on the results of docking studies, researchers can optimise and refine drug molecules to enhance their efficacy. Thiosemicarbazides are a significant component in the pharmaceutical industry, used in organic synthesis for the synthesis of heterocycles. Their broad structural makeup, potential biological applications, multiple bonding mechanisms, and ion-sensing capabilities have garnered significant interest in thiosemicarbazone chemistry [4]. Thiosemicarbazones have a wide range of biological actions against bacteria, fungi, and certain tumours, and are used as treatments [5]. Their actions are influenced by the heteroatomic ring type and the thiosemicarbazone moiety structure [6]. They interact with metal ions to produce anticancer, antiprotozoal, antibacterial, and antiviral effects, making them valuable models for bioinorganic processes [7]. Applications of cholesterol-reducing agents, such as 3-hydroxy-3-methylglutaryl coenzyme A reductase (HMGCR) inhibitors, are often categorised based on their anticancer, antiprotozoal, antibacterial, and antiviral properties, particularly in the treatment of coronary artery disease. Statins significantly reduced the cardiovascular disease burden globally [8,9], but lowering elevated LDL cholesterol levels before statin treatment proved challenging, despite clinical practice guidelines. The study detected HMGCR activity in rat liver peroxisomes for the first time using immunoelectron imaging and enzyme tests. Peroxisome activity was found to be less than 5% in control cells but increased to 30% after cholestyramine treatment. Previous observations of peroxisomal HMGCR in hamster ovary epithelial tissues (CHO cells) are not significant, and it is also well-reported in other tissues [10,11]. The present study on the brominated thiosemicarbazone derivative EBEHC demonstrates several novel features that distinguish it from earlier literature. Unlike conventional works focusing on general synthesis and metal coordination for antimicrobial or anticancer activity such as those by Singh et al. (2005)[12], who synthesized and evaluated metal complexes of thiosemicarbazones, or Mishra et al. (2006)[13], who reported thiosemicarbazone-based Schiff bases and their biological properties, this research presents the first single-crystal XRD structural characterization of EBEHC, revealing a rare $P2_1/c$ space group and unique Br···H and S···H hydrogen bonding. Going beyond basic DFT calculations typically reported, it includes a thorough conformational analysis identifying EBEHC(d) as the most stable conformer with an energy gap of ~3097524.36 kJ/mol. Molecular docking results show EBEHC binds HMG-CoA reductase with a –4.9 kcal/mol score and forms a hydrogen bond with Asp767A, highlighting a novel cholesterol-lowering potential not explored in prior thiosemicarbazone research (Finch et al., 1999). Additionally, ADMET profiling reveals strong pharmacokinetic properties such as high human intestinal absorption (94.76%) and good MDCK cell permeability, positioning EBEHC as a promising lead compound.

2. Sample Preparation

The starting material for EBEHC was synthesised by reacting 1-(4-bromophenyl) ethanone (3.981 g, 0.02 mol) with thiosemicarbazide (1.82 g, 0.02 mol) in absolute methanol (60 mL) within a round-bottom flask. The synthesis utilised commercially available Merck GR materials. Under continuous stirring, the reaction mixture was refluxed for two hours with p-toluenesulfonic acid as a catalyst. The resulting precipitate was filtered, washed thoroughly with cold methanol, and air-dried after cooling to room temperature. To ensure optimal conditions for crystal growth, the growing beaker was kept free from dust and vibrations and covered with a porous material. Yellow single crystals of EBEHC were obtained through recrystallisation in methanol using the slow evaporation method. The reaction scheme for EBEHC is illustrated in Fig. 1.

1H-NMR (DMSO-d6, δ(ppm)): 2.29 (s, H, -CH3), 7.41-7.44 (d, 2H, Ar-H), 7.96-7.99 (d, 2H, Ar-H), 8.0 (s, H, N-H), 8.31(s, H, N-H), 10.26 (s, H, C=N-NH-C) 13CNMR (DMSO-d6, δ(ppm)): 14.31 (CH3), 128.64 (2C, Aromatic), 128.88 (2C, Aromatic), 134.36 (1C , Aromatic), 133.67 (1C, C-Br), 146.90 (1C, C=N), 179.78 (1C, C=S).

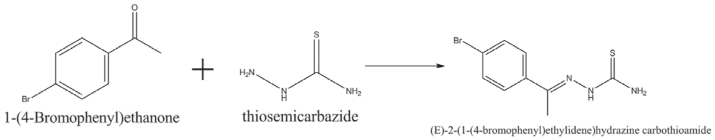

Figure 1: Reaction scheme of EBEHC

3. Characterization Details

Diffraction data for a selected single crystal of EBEHC was collected at room temperature using an Oxford Diffraction X Calibur Gemini S diffractometer equipped with CuKα radiation (λ = 1.5418 Å). The powdered form of EBEHC was employed for recording FTIR and FT-Raman spectra. The infrared spectra of EBEHC, within the range of 4000–400 cm^{-1}, were acquired using a PerkinElmer FT-IR spectrometer, without the use of NaCl plates or KBr pellets in solid form. The FT-Raman spectrum was recorded with a Nexus 670 spectrophotometer using a 1064 nm excitation wavelength, spanning the spectral range of 4000–50 cm^{-1}. Additionally, the UV-Vis absorption spectra of EBEHC in solid form were analysed in the 200–500 nm range using a V-670 UV-VIS-NIR spectrophotometer.

4. Computational Details

The computations for EBEHC at the B3LYP level were conducted using the Gaussian 09W package [14], employing the DFT/6-311++G(d, p) basis set functions. All geometries were optimised using density functional theory (DFT) [15,16], incorporating Becke's three-parameter hybrid functional [17] and the Lee-Yang-Parr correlation functional [18] (B3LYP) with the 6-31G(d, p) basis set. A scaling factor of 0.97 was applied. Vibrational assignments of various bands were analysed using the GaussView tool [19]. AutoDock Tools (ADT) v1.5.4 and AutoDock v4.2 software, developed by the Scripps Research Institute (http://www.scripps.edu/mb/olson/doc/autodock), were utilised for docking studies. Hirshfeld surfaces and their associated two-dimensional fingerprint plots were generated using CrystalExplorer 3.0. The spectra were plotted using Origin 7.5 software [20].

5. Result & Discussion

5.1. Single Crystal X-Ray Diffraction

5.1.1. X-Ray Diffraction Analysis

The compound with the empirical formula $C_9H_{10}N_3BrS$ was subjected to detailed X-ray crystallographic analysis to elucidate its structural properties. The details of the experimental diffraction data collection and refinement, and Hydrogen bonding geometry are shown in Tables 1 and 2. The study revealed that the crystal is a striking yellow, reflecting its unique composition, and crystallises in the monoclinic system with the space group $P2_1/c$. The lattice parameters were determined to be a=9.2620(7) Å, b=14.281(1) Å, c=8.4140(6) Å, and β = 97.437(9)°, resulting in a calculated unit cell volume of 1103.56(14) $Å^3$. This specific arrangement accommodates four formula units (Z = 4) within the unit cell. At a temperature of 293 K, the crystal density was found to be 1.638 g/cm^3, with physical dimensions measured at 0.236 × 0.164 × 0.150 mm^3.

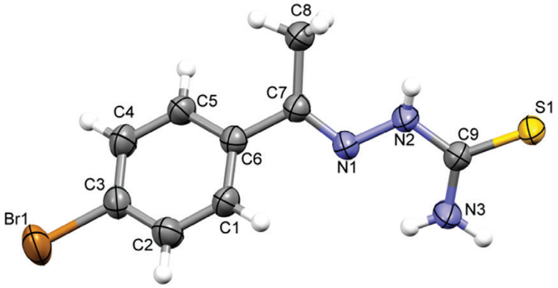

Figure 2: Structure of the EBEHC compound

Data collection employed Mo Kα radiation (λ=0.71073 Å) within a θ range of 2.2° to 27.5°, ensuring comprehensive coverage of reciprocal space. A total of 5169 reflections were recorded, from which 2498 independent reflections were identified (Rint =0.0320). The structure was refined with high precision, achieving an R1 value of 0.0474 and a weighted residual factor (wR_2) of 0.0890 for reflections with I>2σ(I). For all reflections, these values were slightly higher at R1 = 0.0778 and wR_2=0.1010, reflecting the robustness of the dataset. Refinement was carried out using 139 parameters, yielding a goodness-of-fit on F2 of 1.0260, indicative of a well-modelled structure. The largest residual electron density peaks were 0.38 $eÅ^{-3}$ and -0.54 $eÅ^{-3}$, underscoring the accuracy of the electron density map. The Structure of the EBEHC and Crystal packing and intermolecular interactions are shown in Fig.2 and Fig.3.

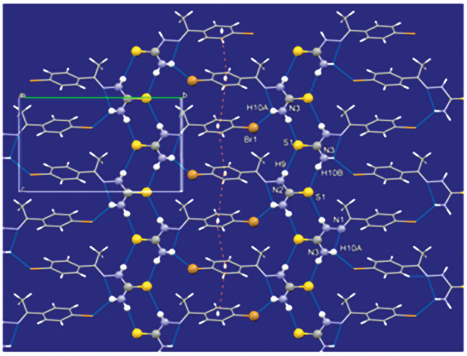

Figure 3: Crystal packing and intermolecular interactions

Table 1: Details of the experimental diffraction data collection and refinement

Empirical Formula	$C_9H_{10}N_3BrS$
Formula weight	272.16
Colour, shape	Yellow
Temperature (K)	293
Crystal size (mm)	0.236 0.164 0.15
Crystal system	Monoclinic
Space group	$P2_1/c$
Lattice constants	
a (Å)	9.2620(7)
b (Å)	14.281(1)
c (Å)	8.4140(6)
β (°)	97.437(9)
Volume (Å^3)	1103.56(14)
Z	4
λ(Å)	0.71073
Calculated density, ρ (g cm^{-3})	1.638
θ range for data collection (°)	2.2-27.5
Absorption coefficient (mm^{-1})	3.879
F(000)	544.0
Reflections collected	5169
Independent reflections	2498 (R(int)=0.0320)
Parameters	139
Goodness-of-fit F^2	1.0260
Final R indices(I>2σ(I))	R1 = 0.0474 wR2 = 0.0890
R indices (all data)	R1 = 0.0778 wR2 = 0.1010
Largest ΔF peak and hole (e Å^{-3})	0.38 and -0.54

Table 2: Hydrogen-bond geometry (Ǻ, o)

D−H•••A	D−H (Å)	H•••A (Å)	D•••A (Å)	D−H•••A (°)
N(3)−H(10b)•••S(1) $^{(i)}$	0.93(3)	2.424(5)	3.341(4)	165.23 (4)
N(3)−H(10a)•••Br(1) $^{(ii)}$	0.83(3)	2.975(4)	3.614(4)	135.30(3)
N(2)−H(9)•••S(1) $^{(iii)}$	1.03(4)	2.785(4)	3.583(3)	176.09(3)
N(3)−H(10a)•••N(1) $^{(iv)}$)	0.83(4)	2.235(4)	2.589 (5)	105.82(2)
Symmetry Codes (i) x,-y+1/2+1,+z+1/2 (ii) x,-y+1/2,+z+1/2 (iii) x,-y+1/2+1,+z-1/2 (iv)x,y,z				

5.1.2. Structural Description

The molecular structure of the compound exhibits a combination of sp^2- and sp^3-hybridizsed carbon and nitrogen atoms, reflecting its intricate bonding pattern. The aromatic ring, comprising six carbon atoms (C1–C6), is planar and consists of sp^2-hybridized carbons, contributing to the delocalized π-electron system. The bromine atom (Br1) is attached to one of these sp^2 -hybridized carbons (C3) in the aromatic ring. The aliphatic carbon atoms C7 and C8 are sp^3-hybridized, forming single bonds with adjacent carbons and hydrogens. The nitrogen atoms (N1, N2, and N3) display varying hybridization states: N1 is sp^2-hybridized as it participates in the planar conjugated system, while N2 and N3 are sp^3-hybridized due to their tetrahedral bonding environments. The sulfur atom (S1) is connected to the sp^3-hybridized carbon (C9), indicating its role in forming a thioether linkage. The structure showcases a balance of planar aromatic and non-planar aliphatic fragments, with the functional groups positioned to allow potential intermolecular interactions, such as hydrogen bonding or halogen bonding, driven by the bromine and nitrogen atoms. This intricate hybridization contributes to the compound's electronic and spatial configuration, potentially influencing its chemical reactivity and physicochemical properties.

5.2. Molecular Structure Analysis

Table 3 provides a detailed comparative analysis of bond lengths and angles derived from experimental (Experimental) measurements and density functional theory (DFT) calculations, emphasising the high consistency between computational predictions and empirical observations. The bond lengths reveal strong concordance, with deviations typically within 0.02 Å, demonstrating the precision of the DFT approach in replicating experimentally determined structural parameters. For instance, the Br1-C3 bond length is observed to be 1.894 Å experimentally and 1.908 Å as predicted by DFT, while the S1-C9 bond length is reported as 1.680 Å experimentally and 1.677 Å computationally. These results underscore the capacity of DFT to capture subtle variations in bond lengths with high fidelity. Similarly, the bond angles exhibit a remarkable level of agreement, with deviations generally constrained to within 3°. Notable examples include the C7-N1-N2 bond angle, measured experimentally at 117.9° and calculated at 119°, and the N3-C9-S1 bond angle, observed at 122.3° experimentally and predicted at 125.02° using DFT. Such close alignment between experimental and theoretical values highlights the robustness of DFT calculations in providing a reliable representation of molecular geometry. This agreement between DFT-predicted and experimental results underscores the effectiveness of computational methods in accurately modelling structural parameters, enabling a deeper understanding of molecular geometries. DFT's ability to account for bond lengths and bond angles with minimal deviations reinforces its applicability as a powerful tool in theoretical chemistry, capable of providing insights into complex molecular systems with a high degree of accuracy and reliability.

Table 3: Optimisation Geometry of EBEHC

Bond Length	**Exp (Å)**	**DFT (Å)**	**Bond Length**	**Exp (Å)**	**DFT (Å)**
Br1 – C3	1.894 (4)	1.908	C3 – C2	1.376 (5)	1.395
S1 – C9	1.680 (4)	1.677	C5 – C4	1.380 (5)	1.393
N1 – C7	1.281 (4)	1.295	C5 – C6	1.383 (5)	1.404
N1 – N2	1.384 (4)	1.356	C7 – C6	1.481 (5)	1.481
N2 – C9	1.356 (4)	1.295	C7 – C8	1.496 (5)	1.511
C9 – N3	1.321 (4)	1.344	C6 – C1	1.384 (5)	1.407
C3 – C4	1.368 (5)	1.391	C1 – C2	1.376 (5)	1.389
Bond Angle	**Exp (°)**	**DFT (°)**	**Bond Length**	**Exp (°)**	**DFT (°)**
C7 – N1 – N2	117.9 (3)	119	N1 – C7 – C6	115.6 (3)	116.51
C9 – N2 – N1	117.5 (3)	121.24	N1 – C7 – C8	124.6 (3)	122.71
N3 – C9 – N2	116.5 (3)	115.06	C6 – C7 – C8	119.8 (3)	120.77
N3 – C9 – S1	122.3 (3)	125.02	C5 – C6 – C1	118.6 (3)	117.97
N2 – C9 – S1	121.2 (3)	119.9	C5 – C6 – C7	121.7 (3)	121.49
C4 – C3 – C2	121.2 (4)	120.82	C1 – C6 – C7	119.7 (3)	120.52
C4 – C3 – Br1	120.0 (3)	119.59	C2 – C1 – C6	121.1 (4)	121.31
C2 – C3 – Br1	118.8 (3)	119.57	C3 – C4 – C5	119.3 (3)	119.28
C4 – C5 – C6	120.8 (4)	121.28	C3 – C2 – C1	119.0 (4)	119.3

5.3. Conformational Analysis

The Energy difference from conformation analysis is shown in Table 4. A comprehensive conformational analysis was conducted to determine the most energetically stable geometry of the synthesised compound. Conformational flexibility is a critical factor in understanding the molecule's chemical behaviour, reactivity, and potential biological activity. In this study, four distinct conformers of the compound, labelled EBEHC(a) through EBEHC(d), were generated and subjected to energy minimisation using computational methods. The electronic energy values were calculated in Hartree units and subsequently converted to kilojoules per mole (kJ/mol) to facilitate interpretation. The energy of the most stable conformer, EBEHC(d), was found to be 1179.7844 Hartree, which corresponds to approximately 3097524.36kJ/mol. This conformer was taken as the reference point for evaluating the relative stabilities of the other structures. Conformer EBEHC(b) exhibited a significantly higher energy of 1169.5209 Hartree (3,070,577 kJ/mol), indicating a destabilisation of approximately 10,311 kJ/mol relative to EBEHC(a). Interestingly, EBEHC(c), with an energy of 1172.3673 Hartree (3,078,051 kJ/mol), appeared to have a negative energy difference of -7473.17 kJ/mol when compared to EBEHC(a). Similarly, EBEHC(d) displayed an energy of 1179.7845 Hartree (3,097,524 kJ/mol), with a reported difference of -19,473.86 kJ/mol. These negative differences are inconsistent with the reference conformer's lowest energy status and suggest either a computational or tabulation artefact. It is plausible that the conversion or labelling may have introduced discrepancies that must be reconciled by referring back to the raw output files or reevaluating the optimisation procedures.

Table 4: Energy difference from conformation analysis

Conformer code	Energy (Hartree)	kJ/Mol	Energy Difference
EBEHC(a)	1173.448132	3080888.31	0
EBEHC2(b)	1169.520891	3070577.33	10310.97229
EBEHC3(c)	1172.367271	3078050.5	-7473.17074
EBEHC4(d)	1179.78447	3097524.36	-19473.8569

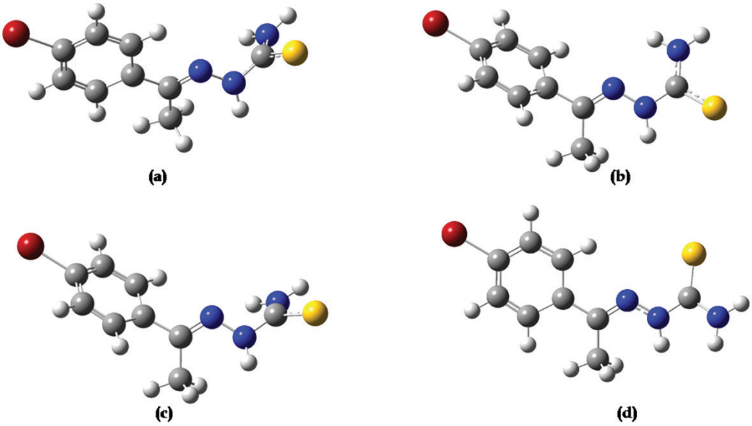

Figure 4: Conformers of EBEHC

5.4. Molecular Electrostatic Potential Analysis

The molecular Electrostatic Potential (MEP) surface is projected over the optimised electronic structure of EBEHC using a density functional B3LYP approach with a 6-31G(d,p) basis set to assess the chemical reactivity of the molecule.

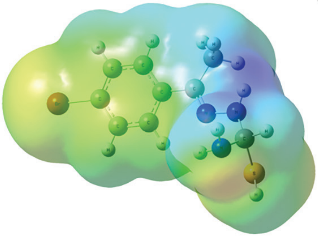

CENTER	CHARGES	CENTER	CHARGES
N1	-0.369492	Br14	-0.132775
N2	-0.438467	H15	0.265400
C3	0.618485	H16	0.355910
S4	-0.283919	H17	0.377763
N5	-0.974044	H18	0.179047
C6	0.601996	H19	0.140428
C7	-0.593121	H20	0.130596
C8	-0.086672	H21	0.055746
C9	-0.082561	H22	0.071020
C10	-0.053772	H23	0.048920
C11	0.084882	H24	0.100097
C12	0.042105	H25	-0.010006
C13	-0.203073	H26	0.155507

Figure 5: MEP Diagram of EBEHC

A powerful tool, the electrostatic potential has been utilised to shed light on the molecular properties of small molecules and their intermolecular association [21], the actions of medicinal compounds and their analogues [22], the biological role of hemoglobin [23], and enzyme catalysis [24]. The probe for detecting reactive sites in molecules is commonly used at both qualitative and semiquantitative levels.

The investigated molecule comprises multiple possible sites for electrophilic (the electrophilic sites are most electronegative and are displayed as red colour) and nucleophilic attack (the nucleophilic sites are most positive and are represented as blue colour). Fig. 5 illustrates that the C3 atom, which is the most electropositive atom in the EBEHC molecules, is charged with 0.618485e. According to the electrostatic potential fitting point charge, the EBEHC molecule has C7 (-0.593121e) as the most electronegative atom.

5.5. Vibrational assignments

The theoretical and experimental FT-IR and FT-Ramanspectrum is shown in Fig. 6 and 7. The theoretical & experimental vibrational wavenumbers (cm^{-1}) calculated using B3LYP/6-31++G(d,p) are shown in Table 5.

(i) N-H vibrations

It has been noticed that the regular recurrence of absorption bands with slightly varying positions from one compound to another may be connected with the occurrence of N-H vibration in a variety of molecules. This is owing to the atomic group's independent vibration and unique frequency inside the molecule. The N-H stretching vibrations occur in the region of 3500-3300 cm^{-1} in all heterocyclic compounds [25]. The N-H vibration occurs with 99% potential energy distribution at 3444 cm^{-1} in FT-IR, 3443 cm^{-1} in FT-Raman, and 3442 cm^{-1} in B3LYP basis set.

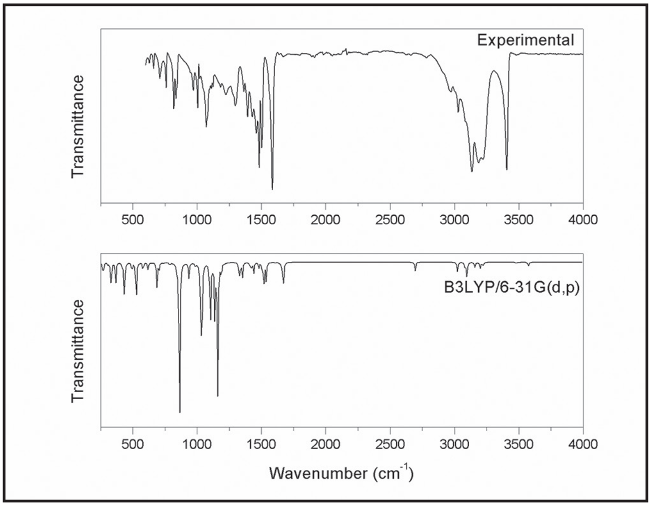

Figure 6: FTIR spectrum of EBEHC

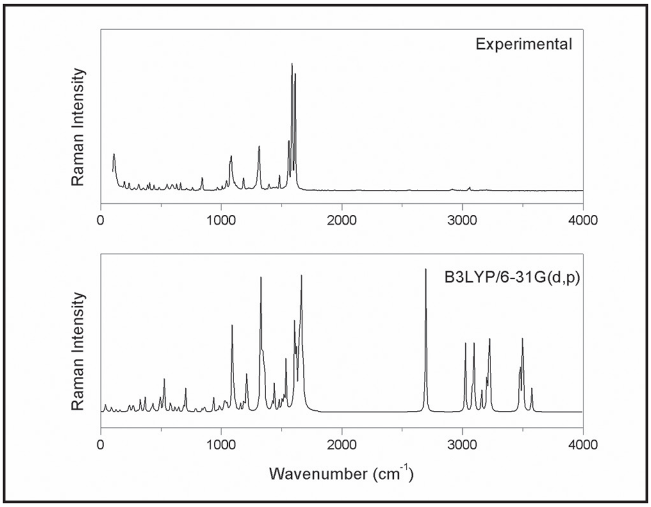

Figure 7: FT Raman spectrum of EBEHC

(ii) C-H vibrations

The C-H stretching vibration is seen in the aromatic structure within the wavelength range of 3100–3000 cm^{-1}, which is the specific region for identifying the C–H stretching vibration. The peaks seen at 3083 and 3045 cm^{-1} in the FT-IR spectrum, and at 3083 and 3048 cm^{-1} in the FT-Raman spectrum, are attributed to the C-H in-plane bending modes in our EBEHC molecule. Theoretical wavenumber, determined using the B3LYP/6-31G(d,p) method, falls within the range of 3082 to 3041 cm^{-1}. The spectral range from 1300 to 1000 cm^{-1} often displays the C-H in-plane bending vibration, which is very advantageous for characterisation purposes.

The band seen at 1097 and 1278 cm^{-1} in the FT-IR spectrum and at 1094 and 1279 cm^{-1} in the FT-Raman spectrum is attributed to the C-H in-plane bending vibration in the present experiment. This band shows a strong correlation with the calculated wavenumber at 1095 and 1277 cm^{-1}. The C-H out-of-plane bending vibrations occur within the frequency range of 1000 to 750 cm^{-1} and are closely associated with vibrations. The C-H out-of-plane bending was seen at 815 cm^{-1} in the FT-IR spectrum and at 816 cm^{-1} in the FT-Raman spectrum. In theory, it has been confirmed using the B3LYP basis set at a frequency of 811 cm^{-1}.

(iii) C-C vibrations

The benzene ring exhibits ring C-C stretching vibrations within the range of 1430-1625 cm^{-1}. Varsanyi[26] reported frequency ranges for the five bands in the region as follows: 1625-1590, 1575-1590, 1470-1540, 1430-1465, and 1280-1380 cm^{-1}.

The FT-Raman bands observed at 1391 and 1582 cm^{-1} and the FT-IR bands detected at 1390 and 1581 cm^{-1} are consequently assigned to C-C vibrations of EBEHC in the present experiment. These values are in remarkable agreement with those expected by B3LYP/6-31G (d, p) at 1387 and 1580 cm^{-1}.

(iv) C-Br vibrations

It is essential to understand the vibrations associated with the connection between the ring and the halogen atoms because this connection enables the vibrations to mix when heavy atoms are present on the edge of the compound[27]. Even though a single carbon atom might include multiple bromine atoms, most aromatic promo compounds absorb strongly in the 650-395 cm^{-1} region. The C-Br stretching vibration is found at the weak mode 445 cm^{-1} in the FT-Raman spectra and 432 cm^{-1} in the B3LYP basis set. The in-plane C-Br bending mode is detected in FT-Raman at 232 cm^{-1} and in the B3LYP basis set at 237 cm^{-1}, respectively. Table 4 shows it.

(v) N-N vibration

When azo compounds are detected by IR spectroscopy, no significant bands are found because the azo group is non-polar [28]. The present study assigns the bands at 1120 and 1114 cm^{-1} in the FT-IR and FT-Raman spectra of EBEHC, respectively, to the N-N stretching mode of vibrations. Band positions for N-N vibrations at 1116 cm^{-1} are represented by the calculated bands at a B3LYP level in the same position.

Table 5: Theoretical & experimental vibrational wavenumbers (cm^{-1}) calculated using B3LYP/6-31++G(d,p)

v_{Raman} cm^{-1}	v_{IR} cm^{-1}	v_{calc} cm^{-1}	IR intensity	Raman activity	Characterization of normal modes with PED (%)
-	-	36	0.4129	6.14937	CCC(31)
-	-	41	1.2115	2.37694	NNC(28)
-	-	51	0.4309	1.46147	CCC(27)+βCCN(17)
-	-	84	0.6997	3.30176	CNN(51)+CCC(25)
-	-	89	0.6630	1.71203	NCN(25)
-	-	123	4.0988	1.99696	HCC(22)+βCCC(16)
-	-	154	1.0545	1.83414	βCNN(15)+βNCS(14)
199	-	203	2.1000	0.34523	CCBr(23)+CNN(20)
-	-	223	1.8393	2.30512	δBrC(35)+δCC(13)
232	-	229	16.207	6.73004	βCCBr(26)
-	-	258	23.399	9.94454	SCN(76)
-	-	293	3.1751	1.08475	βCCBr(15)+γSNN(12)
317	-	316	28.346	9.88403	NCN(35)+ γNNC(14)
-	-	322	13.206	1.82305	βNCS(14)+CCBr(13)
353	-	353	36.100	14.2082	βNCS(25)+γNCN(20)
-	-	402	6.0842	2.50945	δSC(14)+ γSNN(12)
406	-	409	0.3758	1.98125	CCC(42)+CCC(25)
-	-	418	57.110	7.99234	γNCN(14)+βCCN(12)
-	-	432	1.8007	1.40895	δBrC(26)+δcc(18)
475	-	474	15.245	21.4833	βCCN(13)+βCCC(11)
504	-	506	70.575	40.6997	CCC(29)+ γCNH(23)
555	-	558	14.751	12.7451	CCN(37)+CCC(15)
596	-	595	13.679	5.22245	βNCN(18)+δSC(16)
627	626	622	0.8953	6.20595	βCCC(31)+βCCC(21)
662	661	661	43.343	5.46644	δSC(21)+βCNN(10)
679	-	678	10.421	21.7363	γNNC(23)+δSC(20)
712	709	712	1.3955	0.70474	CCC(44)+CCC(33)
760	759	759	5.1591	5.60454	βCCC(19)+δCC(11)
816	815	811	11.427	3.62454	HCC(50)+ γCCH(40)
-	-	828	25.601	4.53444	γCCC(85)
836	835	830	271.48	3.09363	γNHC(35)+δNC(31)
901	-	900	27.056	15.3357	βHSC(58)+ γHCH(10)
-	-	933	0.2278	2.04845	γCCH(52)+CCC(41)
946	947	950	6.1064	7.61513	δCC(33)
961	-	959	0.8362	2.12103	HCC(85)
-	-	984	40.618	9.77934	βCCC(40)+βCCC(21)
-	-	997	181.37	15.0484	δNC(40)+CCC(11)

v_{Raman} cm^{-1}	v_{IR} cm^{-1}	v_{calc} cm^{-1}	IR intensity	Raman activity	Characterization of normal modes with PED (%)
1007	1006	1010	2.2447	7.88344	HCC(40)+CCN(25)
1045	-	1050	6.1127	119.294	vCC(24)
-	-	1061	105.66	22.5731	βCCC(11)
1075	1073	1075	8.3122	12.2884	δNC(36)+ γHCH(14)
1094	1097	1095	92.785	1.68644	βHCC(16)+vNN(64)
1114	1120	1116	220.06	8.54884	vNN(63)
1140	-	1143	22.296	15.3086	γCNN(32)+βHNC(27)
-	--	1167	1.1801	65.7411	βHCC(21)+βHCC(20)
1279	1278	1277	24.040	154.669	γCNN(22)+βHCC(19)+ βHCC(15)
-	-	1282	2.4664	27.8261	βHCC(27)+βHCC(21)+βHCC(14)
1287	-	1287	7.6595	22.7094	vCC(27)
-	1297	1301	23.787	220.761	δCC(18)+ γCNNH(17)
1358	1361	1360	8.9867	4.58374	βHCH(30)+βHCH(27)
1372	-	1371	6.7745	9.13872	βHCN(72)
1391	1390	1387	17.102	30.1363	vCC(20)
1428	1427	1424	8.8837	13.0982	βHNN(54)+βHCH(19)
1441	-	1447	9.0713	12.3776	βHCH(48)+βHNN(23)
1459	1459	1461	42.348	18.5886	βHCH(28)+βHCH(18)
1482	1481	1479	28.634	55.8952	βHCC(14)+βHCH(12)
-		1550	0.7759	107.583	vCC(79)
1582	1581	1580	0.8782	1158.69	vCC(81)
-	-	1599	11.486	8.02653	βHNH(31)
1611	-	1608	44.651	335.817	vNC(73)
2593	2591	2595	14.530	227.904	vSH(98)
2907	2910	2911	14.808	113.095	vCH(90)
2967	2966	2969	11.998	61.2338	vCH(91)
2982	-	2983	23.507	114.630	vCH(97)
3048	3045	3041	9.4553	42.4248	vCH(95)
3082	3083	3082	9.4163	47.7641	vCH(93)
3096	-	3094	0.6236	50.4913	vCH(94)
3104	-	3102	6.0913	107.401	vCH(91)
-	-	3109	1.2409	98.4263	vCH(96)
3343	-	3348	1.5431	133.495	vNH(99)
3372	-	3370	0.4876	223.485	vNH(98)
3443	3444	3442	6.2738	51.6996	vNH(99)

Abbreviations: -Torsion, γ – Out of plane bending, β-Bending, δ-Inplane bending, v-stretching

5.6. Hirshfeld Surface Analysis

The Hirshfeld surface is a figure that shows the shape that a molecule takes up in the crystal structure and can be generated from the electron distribution. The Hirshfeld Surface Analysis produces 2D fingerprint plots [29] that allow one to identify each type of intermolecular contact and calculate their proportional contribution by calculating the area of the surfaces. Hirshfeld surfaces and the corresponding 2-dimensional fingerprint plots were generated using Crystal Explorer 3.0 [30]. The input file for the fingerprint plot should be in the crystallographic information file format. The 2D fingerprint plot is shown in Fig. 9, while the EBEHC's d_{norm}, Shapeindex, and curviness are shown in Fig. 8. On d_{norm} surface plots, there are three separate colours that represent different types of interactions: red, which represents the spot with the maximum electron density; blue; and white, which represents the d_{norm} value of 0. The Hirshfeld surface's shape index can be used to see how adjacent red and blue triangles stack π–π; if neither pair of triangles is present, there are no π–π interactions. Curvedness based on the Hirshfeld surface's local curvature, indicating complementary bumps (blue regions) and hollows (red regions) when two molecule surfaces come into contact.

A value of d_{norm} is either -ve or +ve when intermolecular connections are longer or shorter than rvdW (van de Waals (vdW) radii). Red denotes tighter contacts and a negative dnorm value, blue denotes longer contacts and a positive dnorm value, and white denotes the distance between contacts on the Hirshfeld surface. These colours are used to illustrate the dnorm values. For H…S, H–Br, and H…N interactions, the respective contributions are 7.7%, 6.3%, and 2.1%. All atoms ending in H have the following relative contributions: Br…H 9.9%, S…H 12.5%, N…H 2.7%, C…H 8.3%, and H…H 31.2%.

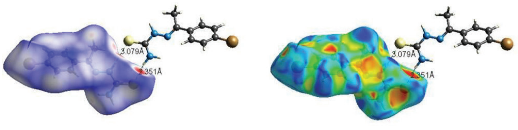

d norm **Shape index**

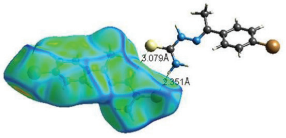

Curvedness

Figure 8: Hirshfeld Surfaces of EBEHC

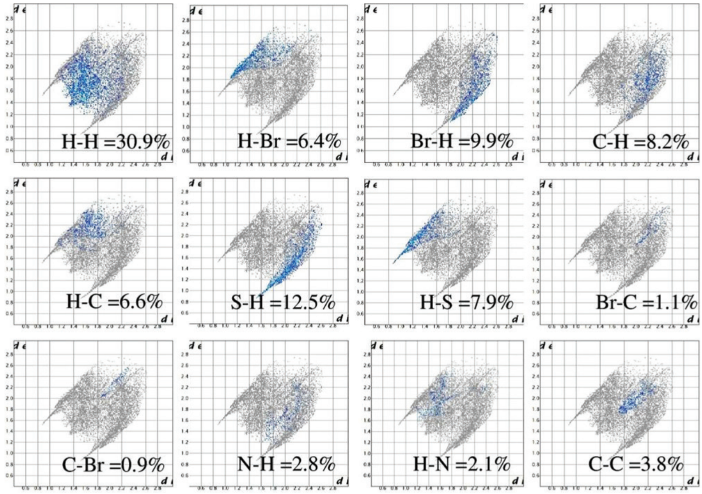

Figure 9: 2D Fingerprint plot of EBEHC

5.7. Frontier Molecular Orbital

The frontier molecular orbital (FMO) analysis provides valuable insights into the electronic properties and reactivity of the molecule. The Highest Occupied Molecular Orbital (HOMO) energy was calculated as 0.667 eV, whereas the Lowest Unoccupied Molecular Orbital (LUMO) energy was −2.696 eV, yielding a frontier molecular orbital energy gap (ΔE) of 3.363 eV. A relatively small HOMO–LUMO gap indicates a molecule with good charge-transfer capability and moderate reactivity, which is favorable in the context of molecular electronics and optoelectronic applications. Moreover, such a gap suggests the compound could undergo excitation under UV or visible light, supporting its applicability in photochemical processes.

This combination facilitates charge transfer interactions, which are often desired in biological activity and molecular docking processes. The HOMO and LUMO surfaces (Fig.10) reveal the electron density distribution over the molecular structure, further indicating the regions of highest chemical activity. The calculated ionisation energy (I) and electron affinity (A) values were 0.667 eV and −2.696 eV, respectively. These values are essential for determining other global reactivity descriptors, including chemical potential (μ), global hardness (η), and electrophilicity index (ω). The chemical potential was computed as −1.014 eV, which represents the tendency of electrons to escape from the equilibrium system. The negative sign indicates a stable electronic configuration, with lower reactivity toward electron loss. The global hardness (η), calculated as −1.681 eV, is theoretically expected to be a positive value. However, the negative value here may be an artefact of the calculation or energy reference, indicating that further correction or validation might be needed.

Moreover, the electrophilicity index (ω), calculated as −0.306 eV, is used to estimate the energy stabilisation. The UV-Vis spectra, both theoretical and experimental (Fig. 11), provide complementary evidence of the molecule's electronic behaviour. The theoretical UV-Vis spectrum, derived using Time-Dependent DFT (TD-DFT) methods, shows absorption bands that align reasonably with the experimental results. The main absorption peak observed in the experimental spectrum is around 285 nm, which correlates with a π→π* transition typically seen in conjugated systems.

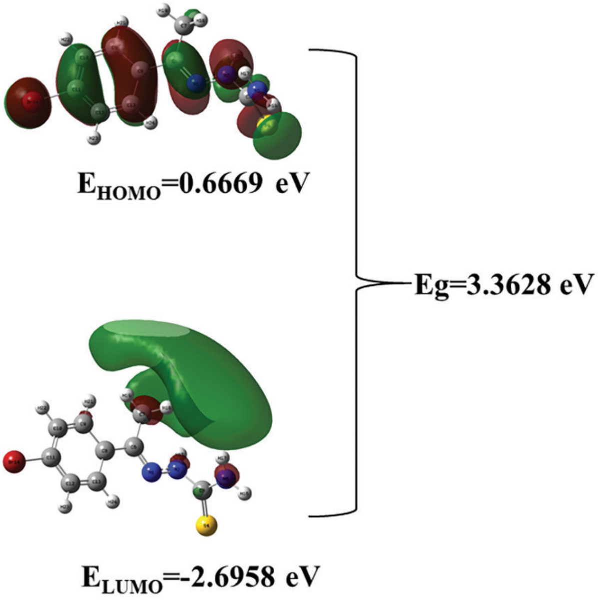

Figure 10: HOMO LUMO of EBEHC

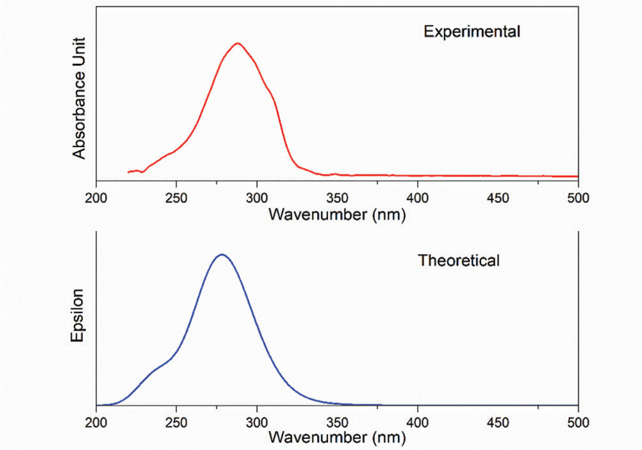

Figure 11: Experimental and Theoretical UV-Vis Spectrum of EBEHC

The TD-DFT simulated spectrum reproduces this feature with a similar 278 nm, confirming the accuracy of the theoretical model and the geometry optimisation. Minor shifts in peak positions between theoretical and experimental spectra may arise due to solvent effects, vibrational broadening, or instrumental conditions not fully accounted for in the simulations.

5.8. Molecular Docking Studies

Through a comprehensive molecular docking investigation, the binding affinities and hydrogen bonding interactions between the ligand and the target protein were examined. The results indicated negative binding affinity values, which suggest potential for favourable interactions under biological conditions. While these preliminary findings are promising, they warrant further experimental validation before drawing definitive conclusions regarding anti-cholesterol activity. Molecular docking, a cornerstone of computer-aided drug discovery, is instrumental in revealing structural and functional compatibility between ligands and target receptors. In the present study, the three-dimensional structure of the ligand EBEHC was generated using ChemDraw Ultra (version 12.0) and subsequently optimised using Gaussian 09W to minimise energy and ensure geometrical stability. The target protein, HMG-CoA reductase (PDB ID: 1DQ8), was retrieved from the Protein Data Bank (http://www.pdb.org). Binding site prediction was carried out using the Q-Site Finder tool, which analyses surface cavities and pocket regions to identify potential active sites.

To ensure computational accuracy and thorough coverage of the active site, the docking grid dimensions were set at 110 × 112 × 110. Such grid optimisation is crucial for enhancing the precision of molecular docking simulations and for applications such as structural comparison and functional site identification. The docking protocol included the addition of polar hydrogens to the ligand to improve interaction specificity, and the flexible ligand EBEHC was docked to the rigid receptor HMG-CoA reductase using the Lamarckian Genetic Algorithm. The parameters were set with a population size of 150 and a mutation rate of 0.02 over ten generations. Notably, the docking simulation revealed a hydrogen bonding interaction between the terminal NH group of EBEHC and the active-site residue Asp767A of the receptor, with a bond length of 1.8 Å, indicating a strong and specific interaction. The binding energy was calculated to be -4.9 kcal/mol, consistent with a potentially favourable interaction. The ligand-receptor complex was visualised using a 2D PoseView diagram (Fig. 12), which offered detailed insights into the interaction pattern. Although these computational findings suggest the potential of EBEHC as a candidate for inhibiting HMG-CoA reductase, experimental studies such as enzyme inhibition assays and in vivo analyses are essential to confirm its therapeutic applicability in cholesterol regulation.

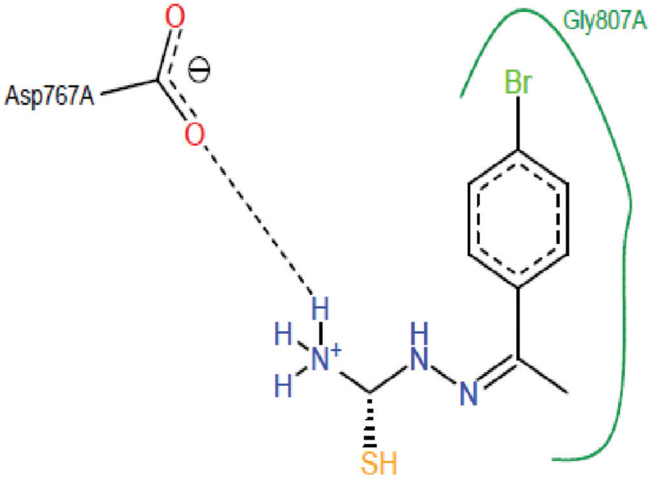

Figure 12: Poseview of EBEHC

5.9. ADMET

The Lipinski Rule (Rule of Five) is followed by the molecule EBEHC. A chemical must have the best ADME characteristics in order to be approved for use in clinical trials. The characteristics of absorption, distribution, metabolism, and excretion (ADME) were evaluated using a web server called PreADME. Usually, only the unbound drug is available for translocation across cell membranes and engagement with a pharmacological target. As a result, a drug's plasma protein binding level has an influence on how effectively it functions, is removed from the body, and is efficacious. Chemicals are securely bound if the value is more than 90%; if not, they are weakly bound. The ranges of well, good, and poor absorption are, respectively, 70-100, 20-70, and 0-20%, according to human intestinal absorption (HIA). The EBEHC measured intestinal absorption at 94.764946%, which is within the range of "well" absorbed in the human gut. Maden Darby Canine Kidney (MDCK) cells exhibit three distinct degrees of cell permeability: low (less than $2.5x10^{-6}$ cm/sec), intermediate (between 2.5 and 50.0x10-6 cm/sec), and high (beyond 50.0x10-6 cm/sec). MDCK cells exhibited a permeability of $23.2604x10^{-6}$ cm/sec in vitro experiments conducted on EBEHC. A direct indicator of drug entrance into the central nervous system is the blood-brain barrier (BBB) (CNS). The three classifications are low, moderate, and high (below 0.1 b/b, 0.1 to 2.0 b/b, and beyond 2.0 b/b). The centralisation of penetration is shown by the BBB's EBEHC rating of 0.80081. For all chemicals utilised in the pharmaceutical, cosmetic, and agricultural industries that come into contact with skin—whether intentionally or accidentally—the skin permeability rate has a major influence on risk management. EBEHC has a skin permeability of -2.01829 cm/hour.

6. Conclusion

The energy prediction on potential EBEHC conformers is carried out in the current work. The most precise theoretical information on the vibrational properties of a single molecule is provided by the DFT approach. The vibrational wavenumbers, infrared intensities, and Raman activities are found, and the EBEHC molecule has undergone a comprehensive vibrational examination. The DFT calculations are carried out at the B3LYP/6-31G (d,p) level. It is shown that the analysis of fingerprint plots generated by the Hirshfeld surface is a valuable method to expedite the recognition of different intermolecular interactions and their relative importance. X-ray diffraction results reveal that the crystal belongs to the monoclinic system. Molecular docking investigations revealed that the synthesised EBEHC molecule has binding modes in the HMG-CoA active site and has a good docking score.

Acknowledgement: I, Dr. R.R. Saravanan, acknowledge the Department of Biotechnology (DBT), New Delhi, India, for their financial support towards research and development under the DBT Star College Scheme.

Conflict of Interest

The authors hereby declare no potential conflicts of interest with respect to the research, funding, authorship, and/or publication of this article

References

1. Yang, R.L., Shi, Y.H., Hao, G., Li, W., Le, G.W., 2008. Increasing oxidative stress with progressive hyperlipidemia in human: Relation between malondialdehyde and atherogenic index. J. Clin. Biochem. Nutr. 43, 154–158. https://doi.org/10.3164/jcbn.2008044
2. Shaik, A.H., Mohammed, A.K., Sammeturi, M., Al Omar, S.Y., Mohammad, A., Kodidhela, L.D., 2020. Maslinic acid ameliorate electrolytes, membrane bound ATPases, antioxidants and histopathology in isoprenaline attenuated myocardial toxicity in rats. J. King Saud Univ. - Sci. 32, 1055–1059. https://doi.org/ 10.1016/j.jksus.2019.09.015
3. Hill, M.F., Singal, P.K., 1996. Antioxidant and oxidative stress changes during heart failure subsequent to myocardial infarction in rats. Am. J. Pathol. 148, 291–300.
4. Mishra, D., Naskar, S., Drew, M.G.B., Chattopadhyay, S.K., 2006. Inorganica Chimica Acta, 359, 585–592. https://doi.org/ 10.1016/j.ica.2005.12.038
5. Labisbal, E., Haslow, K.D., Sousa-Pedrares, A., Valdés-Martínez, J., Hernández-Ortega, S., West, D.X., 2003. Polyhedron, 22, 2831–2837. https://doi.org/10.1016/S0277-5387(03)00361-1
6. Singh, R.V., Fahmi, N., Biyala, M.K., 2005. Journal of the Iranian Chemical Society, 2, 40–46. https://doi.org/10.1007/BF03245978

7. Finch, R.A., Liu, M.C., Cory, A.H., Cory, J.G., Sartorelli, A.C., 1999. Adv. Enzyme Regul. 39, 3–12. https://doi.org/10.1016/S0 065-2571(98)00012-3
8. Bethesda, M.D., 2001. Third Report of the National Cholesterol Education Program (NCEP) Expert Panel… NIH Publication no. 01-3670. https://doi.org/10.1016/S0895-7061(01)02318-8
9. Appelkvist, E.L., Kalen, A., 1989. Biosynthesis of dolichol by rat liver peroxisomes. Eur. J. Biochem. 185, 503–509. https://doi.org/10.1111/j.1432-1033.1989.tb15139.x
10. Hashimoto, F., Hamada, S., Hayashi, H., 1989. Biol. Pharm. Bull. 20, 315–321. https://doi.org/10.1248/bpb.20.315
11. National Collaborating Centre for Primary Care, 2010. NICE Clinical Guideline 67: Lipid Modification.
12. Singh, K., Barwa, M.S., Tyagi, P., 2005. European Journal of Medicinal Chemistry, 40, 1249–1255. https://doi.org/10.1016/j. ejmech.2005.06.016
13. Mishra, A.P., Tiwari, A.K., Singh, M.M., 2006. Journal of the Indian Chemical Society, 83, 577–581.
14. Frisch, M.J., et al., 2009. Gaussian-09, Revision A.01, Gaussian, Inc., Wallingford, CT. Software reference
15. Schlegel, H.B., 1982. J. Comput. Chem. 3, 214. https://doi.org/ 10.1002/jcc.540030212
16. Hohenberg, P., Kohn, W., 1964. Phys. Rev. B 136, 864. https://doi.org/10.1103/PhysRev.136.B864
17. Becke, D., 1993. J. Chem. Phys. 98, 5648. https://doi.org/10.1063/1.464913
18. Lee, C., Yang, W., Parr, R.G., 1988. Phys. Rev. B 37, 785. https://doi.org/10.1103/PhysRevB.37.785
19. Frisch, A., Neilson, A.B., Holder, A.J., 2000. GaussView User Manual, Gaussian, Inc., Pittsburgh. Software manual
20. OriginLab Corp., 2003. Origin 7.5, Northampton, MA. Software
21. Tomasi, J., 1981. In: Politzer, P., Truhlar, D. (Eds.), Chemical Applications of Atomic and Molecular Electrostatic Potentials. Plenum Press, New York, pp. 257–294. https://doi.org/10.1007/978-1-4899-0415-7_11
22. Weinstein, H., Maayani, S., Srebrenik, S., Cohen, S., Sokolovsky, M., 1975. Mol. Pharmacol. 11, 671–689.
23. Perutz, M., 1978. Science 201, 1187–1191. https://doi.org/10.11 26/science.694514
24. Warshel, A., 1981. Acc. Chem. Res. 14, 284–290. https://doi.org/10.1021/ar00068a001
25. Krishnakumar, V., Ramasamy, R., 2008. Spectrochim. Acta A 69, 8–17. https://doi.org/10.1016/j.saa.2007.03.030
26. Varsanyi, G., 1974. Assignments for Vibrational Spectra of Seven Hundred Benzene Derivatives, Adam Hilger. Vols. 1–2. Book

27. Thilagavathi, G., Arivazhagan, M., 2010. Spectrochim. Acta A79, 389–395. https://doi.org/10.1016/j.saa.2010.02.013

28. Yadav, R.A., Singh, I., 2003. Indian J. Pure Appl. Phys. 17, 625. Morgan, K.J., 1961. J. Chem. Soc., 2151–2159. https://doi.org/ 10.1039/JR9610002151

29. Spackman, M.A., Jayatilaka, D., 2009. CrystEngComm 11, 19–32. https://doi.org/10.1039/B818330A

30. Rohl, A.L., Moret, M., Kaminsky, W., Claborn, K., Mckinnson, J.J., Kahr, B., 2008. Cryst Growth Des. 8, 12. https://doi.org/10. 1021/cg070343w